ACS Catalysis

Research Article

pubs.acs.org/acscatalysis

Enhanced Photothermocatalytic Synergetic Activity Toward Gaseous Benzene for Mo+C-Codoped Titanate Nanobelts

Yueli Liu, Wei Shu, Keqiang Chen, Zhuoyin Peng, and Wen Chen*

State Key Laboratory of Advanced Technology for Materials Synthesis and Processing and School of Materials Science and Engineering, Wuhan University of Technology, Wuhan, 430070, P.R. China

Supporting Information

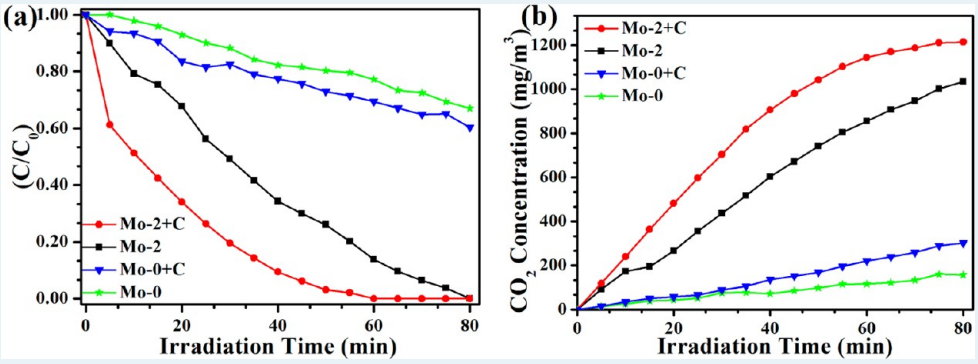

ABSTRACT: In the present paper, a simple and facile method is proposed to synthesize Mo+C-codoped titanate ($H_2Ti_5O_{11}\cdot 3H_2O$) nanobelts by using hydrothermal method together with sol−gel technique, and various Mo-doped and Mo+C-codoped titanate nanobelts are realized by controlling the precursor's contents. It is found that the photocatalytic activity of titanate nanobelts toward gaseous benzene will be greatly enhanced by Mo+C-codoping if comparing with that of the pure titanate nanobelts, Mo-doped titanate nanobelts, and C-doped titanate nanobelts, and the optimal Mo doping content is confirmed to be 0.33 wt % for Mo/Ti ratio. The reason lies in the fact that by Mo+C-codoping (Mo/Ti ratio of 0.33 wt %, C/Ti ratio of 0.33 wt %), the band gap of titanate nanobelts will be narrowed and the allowed paths for photoexcitation will be increased with the generation of impurity energy level, which results in an obvious red-shift in their UV−vis absorption spectra and the increased utilization of the solar energy, and thus enhances their photocatalytic activity. On the basis of the above experimental results, the current photocatalytic mechanism is proposed.

KEYWORDS: *titanate nanobelts, Mo+C-codoped, photocatalytic activity, gaseous benzene*

INTRODUCTION

In recent years, the removing of volatile organic compounds (VOCs) in air is quite important with the increasing attention concerning on the environmental problems,[1] especially for the gaseous benzene, which is considered to be the priority hazardous substance because of its high toxicity, highest cancer risk, confirmed carcinogenicity, and environmental persistence.[2] Therefore, it is quite necessary to develop an efficient and mild route to degrade gaseous benzene from the ambient environment.

As a UV absorber, the titanium dioxide (TiO_2) possesses the main drawback that it only utilizes a small fraction of solar light (about 3−5%).[3] As a TiO_2-derived series, $H_2Ti_nO_{2n+1}$ (n = 3−5) titanate nanomaterials exhibits a monoclinic lattice with parallel corrugated layers of edge-sharing TiO_6 octahedra stepped by every nth octahedral, which is of great interest for photocatalysis since they possess higher optical absorption property than the TiO_2 nanomaterials in visible light region.[4−6] Since the pioneering work by Kasuga et al.,[7,8] alkaline hydrothermal approach has been widely employed to produce various titanates nanomaterials by carefully controlling the hydrothermal conditions, which is varied from tetragonal anatase TiO_2−B,[9] to monoclinic $H_2Ti_3O_7$,[10] orthorhombic lepidocrocite-type $H_{0.7}Ti_{1.8}\square_{0.175}O_{4.0}\cdot H_2O$ ($\square$ = vacancy) naomaterials[11] or $H_4Ti_2O_5\cdot H_2O$ nanotubes.[12] Among them, titanate nanobelts are of particular interest,[13,14] as they have large surface area and may provide the direct transfer path for the photogenerated electrons due to their distinctive geometries, which benefits for the effective separation of the photogenerated electrons and holes during the photocatalytic activity. In our previous work, we first synthesize one-dimensional (1-D) titanate ($H_2Ti_5O_{11}\cdot 3H_2O$) nanobelts.[15]

It is still an important and challenging issue to improve the activities of the photocatalytic system under both of UV and visible light irradiation, as well as making full use of the solar energy. Impurity doping is one of the typical approaches to

Received: July 26, 2012
Revised: October 1, 2012
Published: October 18, 2012

extend the absorption spectral response and enhance the absorption efficiency.[16] Normally, the doping of various transitional metal ions (Bi, Fe, Cr, Co, Mo, V, etc) could shift their optical absorption edge from UV to visible light range.[17,18]Although this approach is able to reduce the band gap of TiO_2 to some extent, the existence of the carrier recombination center and the formation of strongly localized d states within the band gap will reduce the mobility of the charge carriers and limit their further application. Nonmetal (C, N, S, F, B, etc) anion-doping has been reported to show a relatively high level of photocatalytic activity under visible light irradiation, while the monodoping will generate recombination centers inside the photocatalysts, which suppresses the migration of the photoexcited charge carriers to the photocatalysts' surfaces.[19,20] In addition, the formation of the composited TiO_2 nanoheterojunctions (graphene, $LaVO_4$, Fe_2O_3, etc) has been used to widen their optical absorption and photocatalytic activity, while the formed interfaces will be the carrier recombination center.[21,22]

To further improve the photocatalytic activity, codoped TiO_2 with double nonmetal,[23,24] metal−nonmetal,[25,26] metal−metal ion,[27,28] and metal−semiconductor[29] has attracted more attention. Recently, Gai et al. prove that the Mo+C-codoped TiO_2 may be the best candidate for the photocatalytic activity due to their suitable band gap of 2.0 eV by theoretical calculation.[30] In the experiment, Mo+C-codoped TiO_2 film have been synthesized by using thermal oxidation process to enhance the photocatalytic activity of methylene blue solution.[31] Until now, the main drawback lies in the fact that it is quite difficult to control the morphologies and doping concentrations of the Mo+C-codoped TiO_2 nanomaterials, and there is no report for the synthesis of the Mo+C-codoped titanate nanomaterials.

In the present work, a simple and facile method for the synthesis of Mo+C-codoped titanate nanobelts with various Mo doping contents is introduced by using hydrothermal process together with sol−gel technique, which serves as the photocatalysts toward the gaseous benzene.

EXPERIMENTAL SECTION

Synthesis of 1-D Titanate Nanobelts. All of the chemical reagents were analytical grade and used as purchased without further purification (Sinopharm Chemical Reagents Co., Ltd., China). The titanate nanobelts were synthesized by the following hydrothermal process as described in our previous work.[15] 3.33 g commercial TiO_2 powders were dispersed in 100 mL of 10 M NaOH solution with constant stirring, and then the mixed solution was put into a 150 mL of Teflon vessel at 180 °C for 48 h. The as-prepared mixture was repeatedly washed with 0.1 M HCl solution and distilled water in order until the pH value was 5.6, and finally dried at 80 °C overnight, which was marked as Mo-0.

Synthesis of Mo-Doped and Mo+C-Codoped 1-D Titanate Nanobelts. First, the Mo-doped TiO_2 nanoparticles were synthesized by sol−gel technique.[33] Five milliliters of tetra-*n*-butyl titanate was dissolved in 180 mL ethanol solution, then 4.5 mL glacial acetic acid was added, and the pH value was adjusted to be 3.0 by adding concentrated nitric acid with vigorously stirring, and then the ammonium molybdate was added with dissolving in distilled water. After they were stirred for 1 h and sonicated for 1.5 h, the samples were dried at 80 °C overnight and calcinated at 500 °C for 3 h. Then, 3.33 g of the Mo-doped TiO_2 powders synthesized above were used in the same hydrothermal process mentioned in above process to obtain the various Mo-doped titanate nanobelts with the quality ratio between Mo and Ti elements of 0.125%, 0.33%, 0.64%, 1.29%, 5.15%, which were marked as Mo-1, Mo-2, Mo-3, Mo-4, and Mo-5, respectively.

For the case of Mo+C-codoped titanate nanobelts, 3.33 g of Mo-doped TiO_2 powers and excessive glucose (0.2 g, 14.6 mol % for C/Ti ratio) were also dispersed in 100 mL of 10 M NaOH solution; then the same hydrothermal process was followed to obtain the Mo+C-codoped titanate nanobelts, and the various Mo+C codoped samples were marked as Mo-1+C, Mo-2+C, Mo-3+C, Mo-4+C, and Mo-5+C, respectively.

Photocatalytic Activity Experiments. It is found that the photothermocatalytic synergetic effect possesses much higher efficiency than the combination of both photocatalytic and thermal catalytic effect at various temperatures.[34] Photocatalytic degradation of gaseous benzene was conducted using a hermetic stainless steel reactor with 5.0 L volume, and a high-pressure mercury lamp purchased from Philips company (HOK 4/120, output power: 400 W) was installed on a bracket, which has the UV and visible light spectra with the main peak located at the wavelength of 365 nm. The photocatalyst (0.5 g) was dispersed in a thin layer over a glass vessel with the total area of 180 cm^2, which was placed closely to the surface of the irradiation lamp.[35] Therefore, the thermal energy emitted from the lamp leads to their surface temperature automatically increase to 393K measured by a thermal conductivity detector, which may make full use of the light irradiation and nonradiative thermal energy emitted from the irradiation lamp without any additional heater. The required quantity of benzene was injected into the reactor, and the initial concentration of benzene was kept at 370 mg/m^3 for all experiments. Simultaneous determination of the concentration of benzene and carbon dioxide was performed with an online gas chromatograph (GC-9560, Shanghai Chenhua Technology Corp., Ltd., China) equipped with a flame ionization detector, a thermal conductivity detector and a porapak R column. By using terephthalic acid as a probe to analyze the intensity of hydroxyl radicals (•OH), 0.1 g titanate photo catalysts are added into the terephthalic acid solutions (5 mM) containing 10 mM NaOH,[32] which is under mercury lamp light illumination with continuous stirring, and then is taken out for every 5 min with ultrasonic.

Characterization. The morphologies and microstructures of the samples were characterized by using scanning electron microscope (SEM) (Zeiss Ultra-55, ZEISS, German), high-resolution transmission electron microscope (HRTEM) (JEM2100FEF, JEOL, Japan), and X-ray diffractometer (XRD) (PertPro, PANalytical, Netherlands). UV−vis spectra were tested by using Shimadzu UV-2550 spectrophotometer, and •OH-trapping photoluminescence (PL) was tested by using Shimadzu FS-2400 fluorescence spectrometer with the excitation wavelength of 312 nm. X-ray photoelectron spectroscopy (XPS) measurement was performed in the Escalabmk-II XPS apparatus (VG Scientific, England) with Al target. The emission angle between the photoelectron spectra and the sample surface was 45°, and the calibration of the binding energy of the electron spectrometer was made by using the maximum adventitious C1s signal at 284.6 eV with the solution of the full width at half-maximum (fwhm) being 0.8 eV. Specific surface areas of the samples were measured by nitrogen adsorption at 77 K (Micromeritics Tristar ASAP 2020) by using Brunauer−Emmett−Teller (BET) method.

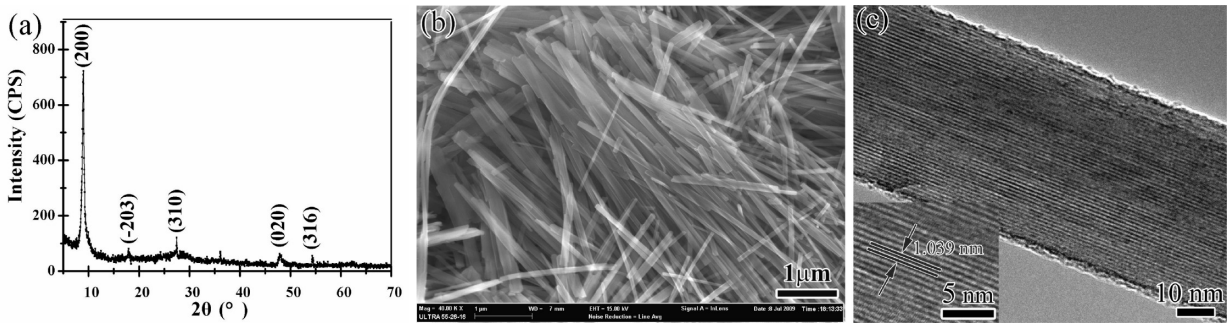

Figure 1. Characteristic of titanate nanobelts: (a) XRD pattern, (b) SEM image, and (c) HRTEM image (magnified HRTEM image inserted).

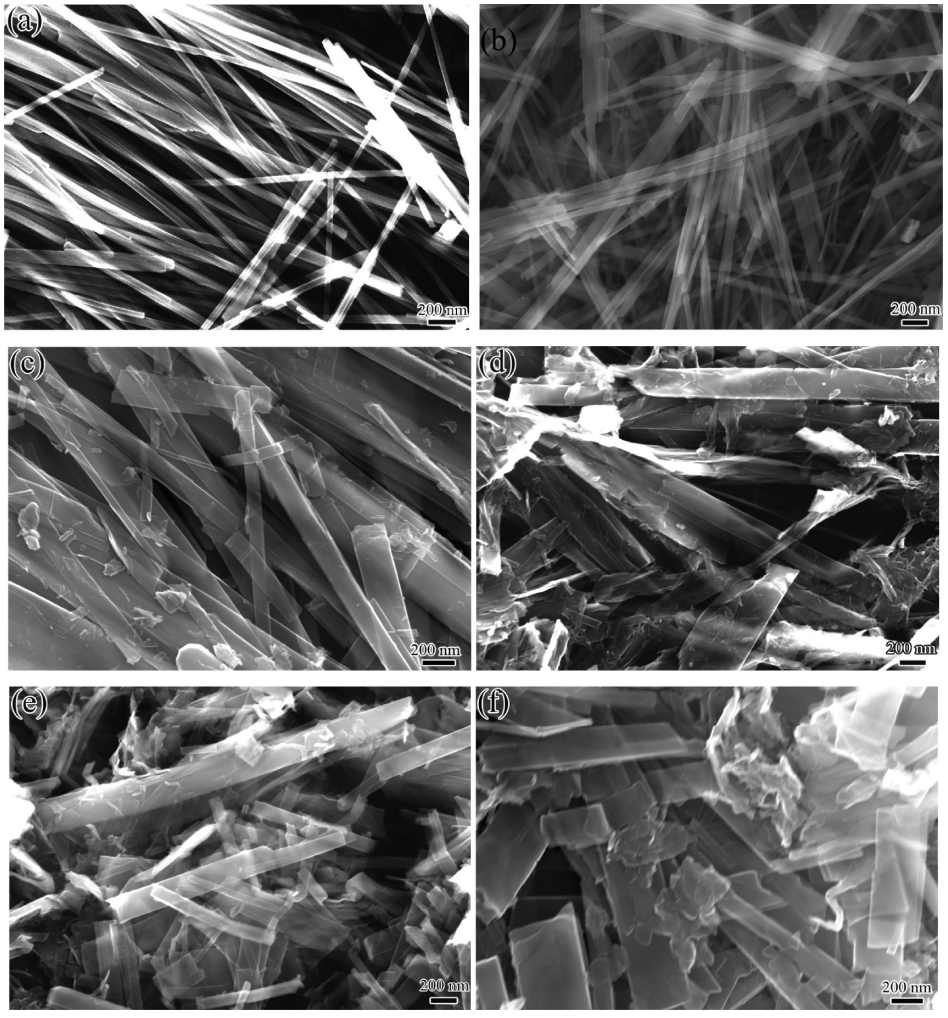

Figure 2. SEM images of the titanate nanomaterials at various Mo doping contents: (a) Mo-2, (b) Mo-2+C, (c) Mo-3, (d) Mo-3+C, (e) Mo-4, and (f) Mo-4+C.

RESULTS AND DISCUSSION

The crystal structure of the as-prepared titanate nanobelts (Mo-0) is proven by the XRD pattern in Figure 1a, which actually contains the peak with 2θ values of 8.9°, and the characteristic peak indicates that the nanobelts are composed of a layered titanate structure and belong to the $H_2Ti_5O_{11}\cdot 3H_2O$ phase (JCPDS No. 44-0130). Figure 1b shows the typical SEM image of as-prepared titanate nanobelts with many homogeneous structures existing, and their width is about 70−80 nm and the length is several micrometers. Further HRTEM image in Figure 1c shows a typical lamellar structure with the straight lattice fringes. To clarify the ordering phenomenon, the magnified HRTEM image inserted in Figure 1c shows that the *d*-spacing normal to the nanobelts along axis is of 1.039 nm, which is consistent with the *d*-value of (200) crystal planes of the monoclinic $H_2Ti_5O_{11}\cdot 3H_2O$.

XRD patterns of the Mo-doped and Mo+C-codoped titanate nanobelts with various Mo doping concentrations are shown in Supporting Information Figure S1, and only titanate phase ($H_2Ti_5O_{11}\cdot 3H_2O$) exists after Mo doping, while titanate phase ($H_2Ti_5O_{11}\cdot H_2O$) also coexists with Mo+C-codoping when the doping contents is over 0.64 wt % in Figure S1b. The fact

dx.doi.org/10.1021/cs300501e | *ACS Catal.* 2012, 2, 2557−2565

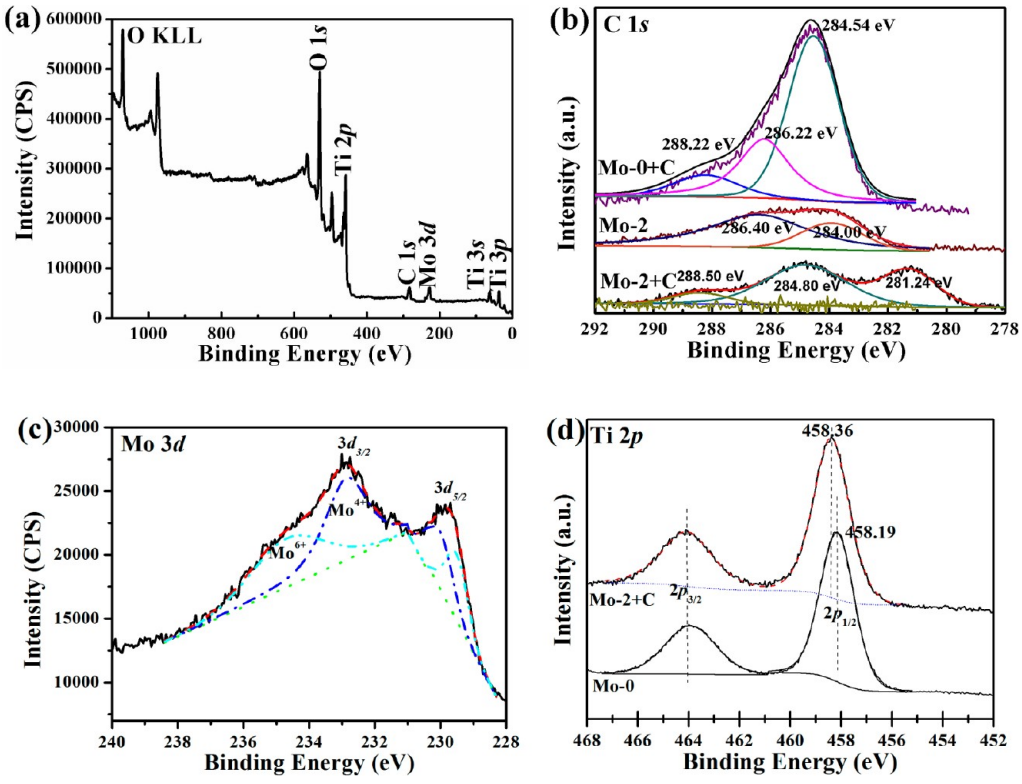

Figure 3. XPS observations of Mo-2+C titanate nanobelts: (a) survey spectrum, (b) C 1s spectrum, (c) Mo 3d spectrum, and (d) Ti 2p spectra of Mo-2+C and Mo-0 titanate nanobelts.

implies that the different doping types and the dopants' contents in this case would not change the titanate phases, and it may only slightly influence its crystal structures over some certain value of dopants.

Figure 2 shows the SEM images of the Mo-doped and Mo +C-codoped titanate nanobelts at various Mo doping contents, which shows that the main morphologies of the doped samples remain belt-like structures. However, with the increasing of the doping content, some of the titanate nanobelts begin to form small sheet-like fraction, which may imply that the morphologies and microstructures of the titanate nanobelts are not thermal stable over some certain content of 1.29 wt % for Mo doping. EDS observation of the Mo-2+C sample in Supporting Information Figure S2a also proves the existence of the Mo, Ti, O, and Na elements with the Mo content of 0.307 wt %. Many reported TiO_2-derived nanotubes seem to actually contain more or less Na ions in spite of the fact that the Na content in TiO_2-derived nanobelts can be decreased by long-term and repeated acid/H_2O washing process. Moreover, the titanate nanobelts have the intrinsic advantage to adsorb and contain the Na element as they have a high ratio between the length to diameter, the surface space and layered structures.[17] FTIR analysis is also used to confirm the atom combination formation of the samples before and after doping, as shown in Supporting Information Figure S2b. The abroad band in the range of 3550−3200 cm^{-1} is the shrinking vibration of O−H bond in the bound of H_2O molecule, and the peak of 1626 cm^{-1} is defined to be the bending vibration of O−H bond. A weak absorption peak of Ti−O bond exists at 897 cm^{-1}, which is in the range of Ti−O−Ti absorption (700−900 cm^{-1}). In the low frequency part of the spectra, many fluctuant bands appear around 500 cm^{-1}, which is attributed to the Ti−O bond. From the FTIR spectra, no changes are found after the Mo+C-codoping for the titanate nanobelts, which implies that the doped Mo and C atoms enter into the crystal lattice instead of existing on the surface of the titanate nanobelts.

XPS results are carried out to study the chemical state of the Mo+C-codoped titanate nanobelts, as shown in Figure 3, which reveals that the samples contain four elements of Ti, O, C, and Mo in XPS survey spectrum in Figure 3a. To investigate the difference of the carbon states in the sample of the Mo-2+C, Mo-2, and Mo-0+C, the C 1s core levels are illustrated in Figure 3b. For the Mo-0+C sample, three peaks with the binding energies of 284.54, 286.22, and 288.22 eV coexist. Generally, the peak at 284.54 eV is a signal of adventitious elemental carbon,[38,39] while the peaks at 286.22 and 288.22 eV are signed to be C−O and C═O bonds in carbonate species (cation C^{4+}-doped), which are formed during the pyrolysis of glucose sucrose and the result of nondehydrated or partially dehydrated carbohydrate species, and it may induce the narrowing of the band gap and response to visible light.[40−42] For the Mo-2 sample, only two peaks with the binding energies of 284.00 and 286.40 eV coexist, which implies that no doped carbon exists in the Mo-doped titanate nanobelts. While for the Mo-2+C sample, three peaks with the binding energies of 284.80, 288.50, and 281.24 eV coexist, and the peak at 288.50 eV implies that the cation C^{4+}-doping in carbonate species exist by the dehydration of the carbohydrate and subsequent carbonization of the formed organic compounds. While the additional peak at 281.24 eV are associated with Ti−C bonds (cation C^{2-}-doped), indicating that carbon substitutes for some of oxygen into the O−Ti−O lattice and forms the O−Ti−C bonds, which could contribute to the red shift of absorption edge to visible light region. The atom content of doped C^{2-} and C^{4+} is estimated to be 1.92% (0.32 wt % for C/Ti ratio) and 0.58% (0.01 wt % for C/Ti ratio), respectively, which is

dx.doi.org/10.1021/cs300501e | ACS Catal. 2012, 2, 2557−2565

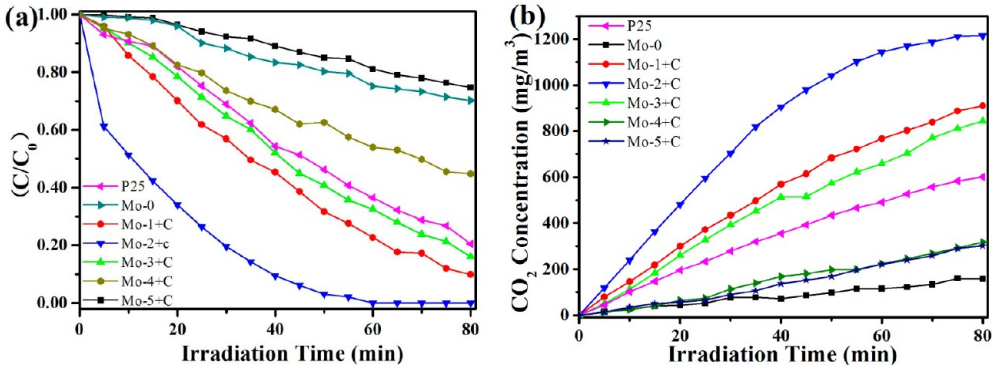

Figure 4. Photodegradation properties of Mo+C-codoped titanate nanobelts at various Mo-doping levels for benzene: (a) Decreasing plots of the benzene concentration and (b) increasing plots of the CO_2 concentration.

multiplied by the C element sensitive factor to all peaks and then multiplied by respective element sensitive factor by comparing the peak area at 281.2 and 288.50 eV. C, C−O, and Ti−C species easily appear on the surface of materials without doping into intercrystal lattice, while in our case there is no existence of the above doped elements on their surface from the FTIR spectra in Supporting Information Figure S2b. Therefore, only a part of C atoms enter into the lattice sites to substitute for O atoms or exist in carbonate specie if comparing with the added C content of 14.6 mol % for C/Ti atom ratio.

The Mo 3d spectrum from Mo 3d core levels proves that the two phases of Mo^{4+} and Mo^{6+} coexist with the locating peaks at 534.68 and 532.87 eV, respectively, and the relative intensity of the peak of 534.68 eV to peak of 532.87 eV is 1.21:1, as shown in Figure 3c. The result shows that most of the doped Mo elements exist as the Mo^{4+} phase, since its chemical state is same with that of Ti^{4+} phase, thus the Mo atom may more easily enter the crystal lattice of the titanate nanobelts and substitute for the corresponding Ti atom comparing with the Mo^{6+} atoms. In addition, the existence of the Mo^{6+} cation doping provide the formation possibility of the C^{2-} cation-doping because C^{2-} cation-doping will keep the charge balance in the case of the Mo^{6+}-doping, while the C-doped sample of Mo-0+C only possesses the formation of carbonate specie (cation C^{4+} doped). Ti 2p spectra in Figure 3d show that 2*p*3/2 peak of Ti element locates at 464.38 eV, and there is no obvious shift in the peak position after the Mo+C codoping. By considering the XRD results in Supporting Information Figure S1, EDS pattern and FTIR spectra in Supporting Information Figure S2, it may be inferred that the Mo and C elements have been doped into the crystal lattices of titanate nanobelts, therefore, the Mo+C-codoping has been realized.

During the hydrothermal process, some of the Ti−O−Ti bonds are broken, an intermediate containing Ti−O−Na and Ti−OH are formed via NaOH treatment. As the strong static interaction between the Na^+ cations and $[TiO_6]$ unit holds the layers together tightly, while OH^- cations result in weakened static interaction between neighboring $[TiO_6]$ octahedral as the ionic radius of OH^- cations is larger than that of the Na^+ cations,[36] which would proceed with rearrangement to form nanosheets of edge-sharing TiO_6 octahedral with Na^+ and OH^- intercalated between the sheets. Since nanosheets do not have inversion symmetry and not stable, with the continuous insertion of OH^- cations, the interlayer distance of the nanosheets is enlarged. As a result, the nanosheets will be spitted into smaller belt-like nanostructures along the layer direction because of internal stress probably until it releases the strain energy, and it will continuously grow to be $Na_2Ti_5O_{11}{\cdot}3H_2O$ nanobelts with the hydrothermal process.[37] At the same time, at the high concentration of the Mo dopant in the hydrothermal process, the strong static interaction between the Na^+ cations and $[Ti(Mo)O_6]$ unit becomes weak and lead to the layers combine less tightly, as the average ionic radius of 0.623 Å for Mo^{4+} and Mo^{6+} phases is larger than that of the Ti^{4+} ion (0.605 Å) if considering the relative contents of Mo^{4+} and Mo^{6+} from the XPS spectrum in Figure 3c. With the C-doping, the strong static interaction is further weakened due to the decreased coulomb interaction between the Na^+ cations and $[Ti(Mo)O(C)_6]$ unit, which is influenced by difference of the ionic radius between C^{2-} ions O^{2-} ions and will lead to the enlarged distance of the interlayer. After hydrothermal reaction, with the washing treatment by HCl treatment, Na^+ ions are gradually exchanged by H^+ ions to form $H_2Ti_5O_{11}{\cdot}3H_2O$ phases, while the $H_2Ti_5O_{11}{\cdot}H_2O$ phases also form due to the enlarged interlayer distances when Mo+C codoping is over a certain value, as shown in the XRD patterns in Supporting Information Figure S1b. Therefore, the strong static interaction by Mo and C doping favors for the stability of the nanosheets, and it also slightly influences the crystal structure with the titanate nanosheets of $H_2Ti_5O_{11}{\cdot}3H_2O$ and $H_2Ti_5O_{11}{\cdot}H_2O$ phases coexisting, as shown in Figure 2d−2f.

By choosing the photodegradation of gaseous benzene as reference materials, we investigated the potential photocatalytic properties of Mo monodoped and Mo+C codoped titanate nanobelts at various Mo doping, respectively. The conversion between the benzene concentration and the concentration of the produced CO_2 gas acts as a function of irradiation time. It is found that the photocatalytic performance will be enhanced by Mo-monodoping or Mo+C-codoping, meanwhile, too excessive Mo-doping (Mo-5) will reduce the photocatalytic properties for Mo monodoping (Supporting Information Figure S3). The degradation results show that the Mo-2+C sample (Mo/Ti ratio of 0.33 wt %, C/Ti ratio of 0.32 wt %) may achieve the best photocatalytic performance for Mo+C codoped titanate nanobelts, as the gaseous benzene will be totally degraded after 60 min under the UV−visible light irradiation, and the produced CO_2 concentration is of 1200 ppm in Figure 4. It is corresponding to a high mineralization ratio ($[CO_2]_{produced}/[C_6H_6]_{converted}$) of 5.1. Such high ratio suggests that about 85% of converted-benzene is completely mineralized to CO_2 and H_2O, and the other 15% of converted-benzene may be degraded to some kinds of incompletely decomposed compounds, such as CO, acthaldehyde and formaldehyde.[38] For comparison, checking the benzene degradation rate of P25,

dx.doi.org/10.1021/cs300501e | *ACS Catal.* 2012, 2, 2557−2565

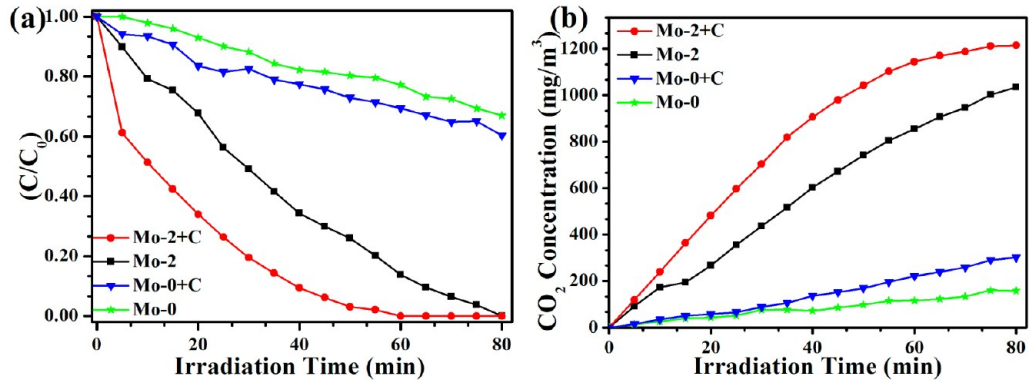

Figure 5. Photodegradation properties of various titanate nanobelts for benzene: (a) Decreasing plots of the benzene concentration and (b) increasing plots of the CO_2 concentration.

the benzene concentration decreases from 370 to 63 mg/m^3 and a concentration of CO_2 (593 mg/m^3) is produced from the benzene photodegradation after 80 min reaction, resulting in a benzene mineralization ratio ($[CO_2]_{produced}/[C_6H_6]_{converted}$) of 2.7. The result suggests that about 45% of converted-benzene is completely mineralized to CO_2 and H_2O, therefore, it is much lower than that of synthesized Mo+C-codoped titanate nanobelts (Mo-2+C).

Morrison has mentioned that the suitable amount of the dopants may capture photogenerated electrons and decrease the recombination rate of photogenerated electron−hole pairs to accelerate photocatalytic reaction.[43] With the increasing of the dopants concentration, electron−hole pairs captured overcome the surface potential barrier and start to be recombined.[44] However, over some certain dopants, the recombination of the photoinduced charge carriers dominates in the reaction comparing with their charge carriers separation, as the dopants concentration is over optimal concentration, the distance between the trap sites will be reduced, and then charge capturing centers maybe become the recombination centers, which leads to the recombination rate increasing exponentially and reduces the photocatalytic activity.[45] At the same time, when the dopants are too excessive, the substitute for Mo^{4+} (or Mo^{6+}) ions from Ti^{4+} crystal lattice leads to the thermal instability in microstructures and to form titanate nanosheets as shown in Figure 2, which will reduce its photocatalytic properties in Figure S3 (Mo-5). In the present experiment, the optimal content of Mo doping is confirmed to be of 0.33 wt % for the Mo/Ti ratio.

Moreover, the photocatalytic activity of a photocatalyst is usually influenced by their morphologies and microstructures, which influences the adsorption of the reactants, the separation ratio of photogenerated electron−hole pairs, and their transporting rate in the catalyst.[46] The photogenerated charge carriers in titanate nanobelts not only possess strong redox ability but also are long-lived enough to react with the surface absorbed H_2O and O_2 to form strong oxidizing species, such as ·OH and $\cdot O_2^-$, which may degrade benzene efficiently.

We have also measured the ·OH-trapping photoluminescence (PL) spectra using terephthalic acid as a probe to analyze the intensity of hydroxyl radicals (·OH) over Mo-0, M0−0+C, Mo-2, and Mo-2+C. Supporting Information Figure S4a shows the typical changes in the PL spectra with irradiation time in the presence of Mo-2+C, and it is clear that the PL intensity at about 426 nm increases gradually with the illumination time. The ·OH radicals produced over the photocatalysts surface are proportional to the light irradiation time in Supporting Information Figure S4b, which obeys zero-order reaction rate kinetics.[32] As clearly noted in Supporting Information Figure S4b, the order of the formation rate of ·OH radicals is followed: $r_{Mo\text{-}2+C} > r_{Mo\text{-}2} > r_{Mo\text{-}0+C} > r_{Mo\text{-}0}$, which shows that the Mo-2+C titanate nanobelts have the best photocatalytic activity.

The Brunauer−Emmett−Teller (BET) surface areas of the titanate nanobelts (Mo-2+C) and the titanate nanosheets (Mo-4+C) are determined by N_2 adsorption using an ASAP-2020 surface area analyzer (Figure S5), which shows that the titanate nanobelts possess higher specific surface areas (57.51 m^2/g) than that of the titanate nanosheets (43.38 m^2/g). Therefore, the large surface area of titanate nanobelts in Figure 2a−2c is more favorable for the adsorption of benzene due to their larger surface area if comparing with the titanate nanosheets in Figure 2d−2f. As a larger amount of benzene molecules absorbed on the surface, it becomes more easy for the pollutants to react with the active species (·OH and $\cdot O_2^-$) generated both on the catalyst outer surface and inner channels, and this may be another important reason for the high activity of the titanate nanobelts (Supporting Information Figure S3 and Figure 4).

To compare the effect of the photodegradation rate for different dopants, the optimal Mo doping content of 0.33 wt % is chosen for the Mo/Ti ratio, and the corresponding photocatalytic properties are listed in Figure 5. It is shown that the photodegradation rate of the gaseous benzene for the Mo-0 titanate nanobelts is to be 32% after 80 min under the UV−visible light irradiation in Figure 5a, and the produced CO_2 concentration is only of 166 ppm in Figure 5b. The photodegradation rate of the gaseous benzene for the Mo-0+C titanate nanobelts is to be 41% after 80 min under the UV−visible light irradiation, and the produced CO_2 concentration is only of 309 ppm. However, the gaseous benzene will be totally degraded by Mo-2 titanate nanobelts after 80 min, while the total photodegradation time only needs 60 min for the Mo-2+C titanate nanobelts, and the corresponding produced CO_2 concentration is of 1000 and 1200 ppm, respectively. From the above results, it proves that the photocatalytic activities of the titanate nanobelts will be greatly enhanced by Mo+C-codoping.

UV−visible spectra are used to character the optical absorption of all of the above samples in the wavelength range of 300−800 nm (Supporting Information Figure S6). It shows that by Mo-doping the absorption edge of all samples will shift to the visible light range comparing with that of the pure titanate nanobelts (Mo-0) for either Mo-monodoping or

dx.doi.org/10.1021/cs300501e | ACS Catal. 2012, 2, 2557−2565

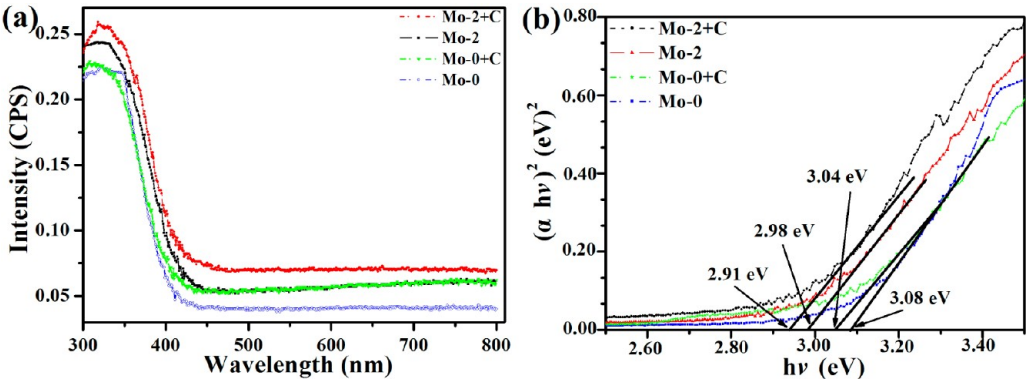

Figure 6. Optical absorption properties of various titanate nanobelts: (a) UV−vis spectra and (b) energy gap calculated by plots for $(\alpha h\nu)^2$ versus $h\nu$.

Mo+C-codoping, which is related to the narrowing band gap by doping. However, for the samples with too excessive Mo doping contents, the absorption intensity will be reduced in UV light range even in visible light range (Mo-5), and then the photocatalytic performance will also be reduced. Interestingly, the absorption intensity of titanate nanobelts is higher than that of the P25 in visible light region while it is lower in UV light region in Supporting Information Figure S6b. To clearly illustrate the changed detail, we choose to list the UV−vis spectra of some samples (Mo-0, Mo-0+C, Mo-2, Mo-2+C) in Figure 6a. In UV region, the absorption intensity of the Mo-2+C titanate nanobelts is higher than that of Mo-0, Mo-0+C, and Mo-2 titanate nanobelts. As the concentration of oxygen vacancies formed during the synthesis process has important effect on the UV absorption,[45−49] and the substitution for C^{2-} and C^{4+} ions from O^{2-} crystal lattices by C-doping might favor for the stability of the oxygen vacancies. In the visible light region, owing to the existence of Mo+C-codoping, the optical absorption enhances significantly if comparing with that of the pure, C-doped and Mo-doped titanate nanobelts. However, there is no obvious optical absorption peak in the visible light region. In addition, it shows that their absorption edges behavior red-shift to about 427, 416, and 407 nm for the Mo-2+C, Mo-2, and Mo-0+C titanate nanobelts in Figure 6a, respectively, by comparing with that of Mo-0 titanate nanobelts (402 nm).

Normally, optical band gap (E_g) may be obtained by the extrapolation of the linearized formulation of the Tauc equation[50] as

$$\alpha h\nu = A(h\nu - E_g)^{1/2} \quad (1)$$

Here, α is the absorption coefficient, $h\nu$ is the photon energy, A is the constant. Therefore, the band gap (E_g) of the titanate nanobelts with or without doping may be inferred from the UV−vis absorption spectra in Figure 6a by the Tauc equation, as shown in Figure 6b. It shows that the band gap of the Mo-0+C, Mo-2, and Mo-2+C titanate nanobelt is calculated to be 3.04, 2.98, and 2.91 eV, respectively, which is narrowed and then induces the obvious optical absorption in visible light region by comparing with that of the Mo-0 titanate nanobelts (3.08 eV).

The Mo 3d orbital energy is calculated to be 1.2 eV and lower than that of Ti 3d orbital energy, when the Mo atom substitutes for the Ti lattice site, the defect levels are generated under 0.10 eV of the titanate's band gap by overlapping Ti 3d orbital level and 3d Mo orbital level in Figure 7, which causes

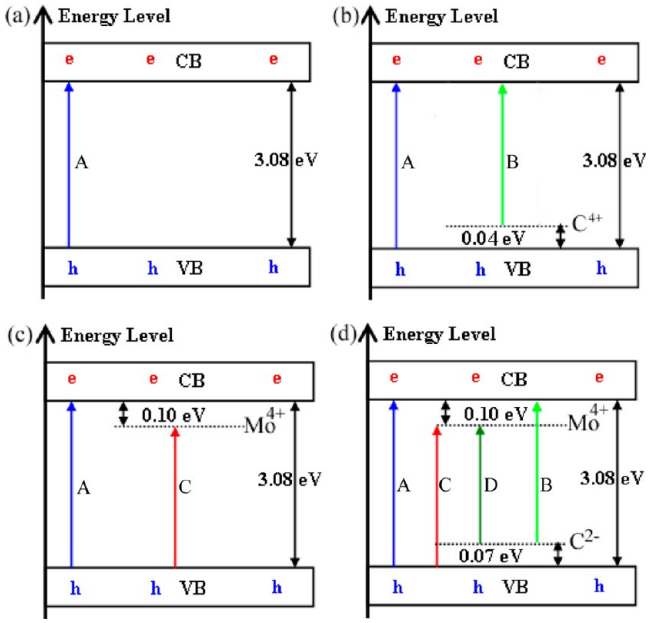

Figure 7. Schematic diagram of the band gap of various samples: (a) Mo-0 titanate nanobelts, (b) Mo-0+C titanate nanobelts, (c) Mo-2 titanate nanobelts, and (d) Mo-2+C titanate nanobelts.

little perturbation at the conducting band minimum (CBM) and leads to the absorption-edge shifting to the visible light range.[27] On the other hands, the monodoped Mo creates partially occupied impurity bands that can facilitate the formation of recombination centers, and thus reduces the photoelectrochemical efficiency, such as the photocatalytic property of Mo-5 (Supporting Information Figure S3).[31] Using charge compensated donor−acceptor pairs with the Mo+C codoping will solve the above problem, as the electrons on the donor levels passivate the same amount of holes on the acceptor levels, and thus the doped systems still keep semiconductor character. As the p-type dopant, C-doping with C^{2-} and C^{4+} cations in Mo-2+C sample may form a new impurity state lying above the valence band of titanate nanobelts with 0.07 eV, as shown in Figure 7. Compared with the Mo-0 and Mo-0+C samples, the band gap has the value shift of 0.04 eV, which is induced by the existence of carbonate specie, and then the band gap will be further narrowed with the C^{2-} cation-doping. It will further decrease the band gap of titanate nanobelts and increase the absorption of the visible light.[31] Therefore, the C^{2-} (or C^{4+}) and Mo^{4+} (or

dx.doi.org/10.1021/cs300501e | ACS Catal. 2012, 2, 2557−2565

Mo^{6+}) ion-doping induces the generation of new states nearing to the valence band and conduction band of the titanate nanobelts, respectively. The synergistic effect of the C^{2-} (or C^{4+}) and Mo^{4+}(or Mo^{6+}) ions leads to the much narrowing of the band gap and greatly improves the photocatalytic activity in the visible light region and thus inhibits the recombination of the photogenerated electron−hole pairs, as proven by the photodegradation results in Figure 5 and UV−vis absorption spectra in Figure 6.

Illustrated in Figure 7, by Mo+C codoping, the electron produces under the irradiation by UV light may be excited from the valence band to the conduction band (process A) or from the valence band to the Mo impurity level (process B) or from the C impurity level to the Mo impurity level (process C) or from the carbon impurity level to the conduction band (process D). However, under the visible light irradiation, the electron can not only be generated from process A for the pure titanate nanobelts but also from the other three processes (process B, C, and D). Therefore, the improvement of the photocatalytic activity by Mo+C-codoping is due to the band gap narrowing and the enhancement of the utilization efficiency of solar energy.[31]

CONCLUSIONS

Mo+C-codoped titanate nanobelts are successfully synthesized by combining hydrothermal method and sol−gel technique, and used in the photodegradation toward the gaseous benzene. It is found that the photocatalytic activity of Mo+C-codoped titanate nanobelts toward gaseous benzene will be totally degraded in 60 min, which is greatly enhanced if comparing with that of the pure titanate nanobelts, C-doped titanate nanobelts, and Mo-doped titanate nanobelts, and the optimal Mo-doping content is confirmed to be 0.33 wt % for Mo/Ti ratio. With the optimal contents for Mo+C codoping (Mo/Ti ratio of 0.33 wt %, C/Ti ratio of 0.32 wt %), the band gap of titanate nanobelts will be narrowed with the generation of impurity energy level, which leads to the existence of an obvious phenomenon of red-shift in their absorption spectra. At the same time, the extra allowed photoexcited paths will be generated and increase the utilization efficiency of solar energy by Mo+C-codoping. Therefore, the photocatalytic activity is greatly enhanced.

ASSOCIATED CONTENT

Supporting Information

XRD patterns, EDS patterns, FTIR spectra, photodegradation properties, ·OH trapping PL spectra, fluorescence intensity, nitrogen adsorption−desorption isotherms, and optical absorption properties. This material is available free of charge via the Internet at http://pubs.acs.org.

AUTHOR INFORMATION

Corresponding Author

*Fax: (86) 27 8765 1107. Tel: (86) 27 8776 0129. E-mail: chenw@whut.edu.cn.

Author Contributions

The manuscript was written through contributions of all authors. All authors have given approval to the final version of the manuscript.

Notes

The authors declare no competing financial interest.

ACKNOWLEDGMENTS

This work is supported by the National Basic Research Program of China (No. 2009CB939704), Defense Industrial Technology Development Program (No. B1420110168), the National Nature Science Foundation of China (No. 51072152, the A3 Foresight Program-No. 51161140399), Science-Technology Chenguang Foundation for Young Scientist of Wuhan (201150431087), and the Fundamental Research Funds for the Central Universities (2012-IV-007).

REFERENCES

(1) Ao, C. H.; Lee, S. C.; Mak, C. L.; Chan, L. Y. *Appl. Catal., B* **2003**, *42*, 119−224.
(2) Hou, Y.; Wu, L.; Wang, X.; Ding, Z.; Li, Z.; Fu, X. *J. Catal.* **2007**, *250*, 12−18.
(3) Fujishima, A.; Honda, K. *Nature* **1972**, *238*, 37−38.
(4) Tang, Z. R.; Zhang, Y. H.; Xu, Y. J. *ACS Appl. Mater. Interf.* **2012**, *4* (3), 1512−1520.
(5) Li, Q. Y.; Kako, T.; Ye, J. H. *Appl. Catal., A* **2010**, *375* (1), 85−91.
(6) Song, H. Y.; Jiang, H. F.; Liu, T.; Liu, X. Q.; Meng, G. Y. *Mater. Res. Bull.* **2007**, *42* (2), 334−344.
(7) Kasuga, T.; Hiramatsu, M.; Hoson, A.; Sekino, T.; Niihara, K. *Langmuir* **1998**, *14*, 3160−3163.
(8) Kasuga, T.; Hiramatsu, M.; Hoson, A.; Sekino, T.; Niihara, K. *Adv. Mater.* **1999**, *11*, 1307−1311.
(9) Sasaki, T.; Watanabe, M.; Michiue, Y.; Komatsu, Y.; Izumi, F.; Takenouchi, S. *Chem. Mater.* **1995**, *7*, 1001−1007.
(10) Jr, E. M.; de Abreu, M. A. S.; Moure, G. T.; Marinkovic, B. A.; Jardim, P. M.; Araujo, A. S. *Chem. Mater.* **2007**, *19*, 665−676.
(11) Sasaki, T.; Watanabe, M. *J. Am. Chem. Soc.* **1998**, *120*, 4682−4689.
(12) Zhang, H.; Li, G. R.; An, L. P.; Yan, T. Y.; Gao, X. P.; Zhu, H. Y. *J. Phys. Chem. C* **2007**, *111*, 6143−6148.
(13) Wang, Y. M.; Du, G. J.; Liu, H.; Liu, D.; Qin, S. B.; Wang, N.; Hu, C. G.; Tao, X. T.; Jiao, J.; Wang, J. Y.; Wang, Z. L. *Adv. Funct. Mater.* **2008**, *18*, 1131−1137.
(14) Zhou, W. J.; Liu, H.; Wang, J. Y.; Liu, D.; Han, S. J.; Lin, J. J.; Wang, R. J. *Phys. Chem. Chem. Phys.* **2010**, *12*, 15119−15123.
(15) Liu, Y. L.; Zhong, L.; Peng, Z. Y.; Cai, Y.; Song, Y. B.; Chen, W. *CrystEngComm* **2011**, *13*, 5467−5473.
(16) Clifford, N.; Palomares, E.; Nazeeruddin, K.; Thampi, R.; Grätzel, M.; Durrant, J. R. *J. Am. Chem. Soc.* **2004**, *126*, 5670−5671.
(17) Hu, Y.; Cao, Y. T.; Wang, P. X.; Li, D. Z.; Chen, W.; He, Y. H.; Fu, X. Z.; Shao, Y.; Zheng, Y. *Appl. Catal., B* **2012**, *125*, 294−303.
(18) Nagaveni, K.; Hegde, M. S.; Madras, G. *J. Phys. Chem. B* **2004**, *108*, 20204−20212.
(19) Wang, J.; Tafen, D. N.; Lewis, J. P.; Hong, Z. L.; Manivannan, A.; Zhi, M. J.; Li, M.; Wu, N. Q. *J. Am. Chem. Soc.* **2009**, *131*, 12290−12297.
(20) Xu, Y. J.; Zhuang, Y. B.; Fu, X. Z. *J. Phys. Chem. C* **2010**, *114* (6), 2669−2676.
(21) Zhang, Y. H.; Tang, Z. R.; Fu, X. Z.; Xu, Y. J. *ACS Nano* **2010**, *4*, 7303−7314.
(22) Huang, H. J.; Li, D. Z.; Lin, Q.; Zhang, W. J.; Shao, Y.; Chen, Y. B.; Sun, M.; Fu, X. Z. *Environ. Sci. Technol.* **2009**, *43*, 4164−4168.
(23) Zhou, X. S.; Peng, F.; Wang, H. J.; Yu, H.; Yang, J. *J. Solid State Chem.* **2011**, *184*, 134−140.
(24) Yang, G. D.; Jiang, Z.; Shi, H. H.; Jones, M. O.; Xiao, T. C. *Appl. Catal., B* **2012**, *96*, 458−465.
(25) Cong, Y.; Zhang, J. L.; Chen, F.; Anpo, M.; He, D. N. *J. Phys. Chem. C* **2007**, *111*, 10618−10623.
(26) Hamadanian, M.; Reisi-Vanani, A.; Majedi, A. *Appl. Surf. Sci.* **2010**, *256*, 1837−1844.
(27) Zhang, D. R.; Kim, Y. H.; Kang, Y. S. *J. Curr. Appl. Phys.* **2006**, *6*, 801−804.
(28) Khan, R.; Kim, S. W.; Kim, T. J.; Nam, C. M. *Mater. Chem. Phys.* **2008**, *112*, 167−176.

(29) Yang, X.; Xu, L.; Yu, X.; Guo, Y. *Catal. Commun.* **2008**, *9*, 913−918.
(30) Gai, Y. Q.; Li, J. B.; Li, S. S.; Xia, J. B.; Wei, S. H. *Phys. Rev. Lett.* **2009**, *102*, 036402.
(31) Zhang, J.; Pan, C. X.; Fang, P. F.; Wei, J. H.; Xiong, R. *ACS Appl. Mater. Interf.* **2010**, *2* (4), 1173−1176.
(32) Zhang, Y. H.; Tang, Z. R.; Fu, X. Z.; Xua, Y. J. *Appl. Catal., B* **2011**, *106*, 445−452.
(33) Negishi, N.; Iyoda, T.; Hashimoto, K.; Fujishima, A. *Chem. Lett.* **1995**, *9*, 841−842.
(34) Li, Y. Z.; Huang, J. C.; Peng, T.; Xu, J.; Zhao, X. J. *ChemCatChem* **2010**, *2*, 1082−1087.
(35) Du, J. J.; Chen, W.; Zhang, C.; Liu, Y. L.; Zhao, C. X.; Dai, Y. *Chem. Eng. J.* **2011**, *170*, 53−58.
(36) Yang, J. J.; Jin, Z. S.; Wang, X. D.; Li, W.; Zhang, J. W.; Zhang, S. L.; Guo, X. Y.; Zhang, Z. J. *Dalton Trans.* **2003**, *20*, 3898−3901.
(37) Zhang, D. R.; Kim, C. W.; Kang, Y. S. *J. Phys. Chem. C* **2010**, *114*, 8294−8301.
(38) Ren, W.; Ai, Z.; Jia, F.; Zhang, L.; Fan, X.; Zou, Z. *Appl. Catal., B* **2007**, *69*, 138−144.
(39) Irie, H.; Watanabe, Y.; Hashimoto, K. *Chem. Lett.* **2003**, *32*, 772−773.
(40) Wang, P. H.; Yap, P. S.; Lim, T. T. *Appl. Catal., A* **2011**, *399*, 252−261.
(41) Zhong, J.; Chen, F.; Zhang, J. L. *J. Phys. Chem. C* **2010**, *114*, 933−939.
(42) Chen, C.; Long, M. C.; Zeng, H.; Cai, W. M.; Zhou, B. X.; Zhang, J. Y.; Wu, Y. H.; Ding, D. W.; Wu, D. Y. *J. Mol. Catal. A* **2009**, *314*, 35−41.
(43) Morrison, S R. In *The Chemical Physics of Surface*, 1st ed.; Zhao, B. Y., Liu, Y. J., Bu, N. Y., Eds.; Springer-Verlag: New York, 1990; Vol. *326*, p 322.
(44) Yang, Y.; Li, X. J.; Chen, J. T.; Wang, L. Y. *J. Photochem. Photobiol. A* **2004**, *163*, 517−522.
(45) Zhang, P. Y.; Yu, G.; Jiang, Z. P. *Adv. Environ. Sci.* **1997**, *5* (3), 1−10.
(46) Chang, W. K.; Rao, K. K.; Kuo, H. C.; Cai, J. F.; Wong, M. S. *Appl. Catal., A* **2007**, *321* (1), 1−100.
(47) Blasco, T.; Camblor, M. A.; Corma, A. *J. Am. Chem. Soc.* **1993**, *115*, 11806−11813.
(48) Yi, J. J.; Yu, P.; Xu, X. X. *Acta Polym. Sin.* **2001**, *3*, 342−346.
(49) Zhang, S. L.; Li, W.; Jin, Z. S.; Zhang, Z. J.; Du, Z. L. *J. Solid State Chem.* **2004**, *177*, 1365−1371.
(50) Robertson, J. *Philos. Mag. B* **1991**, *63*, 47−77.

NOTE ADDED AFTER ASAP PUBLICATION

This paper was published online November 1, 2012. A correction was made to Figure 3b, and the corrected version was reposted November 28, 2012.